nature materials

SUPPLEMENTARY INFORMATION

DOI: 10.1038/NMAT4491

Tunable spin polarization and superconductivity in engineered oxide interfaces

D. Stornaiuolo [1,2*], C. Cantoni [3], G. M. De Luca [1,2], R. Di Capua [1,2], E. Di. Gennaro [1,2], G. Ghiringhelli [4], B. Jouault [5], D. Marrè [6], D. Massarotti [1,2], F. Miletto Granozio [2], I. Pallecchi [6], C. Piamonteze [7], S. Rusponi [8], F. Tafuri, [2, 9] and M. Salluzzo [2 **]

[1] Dipartimento di Fisica, Università di Napoli "Federico II", Complesso Monte Sant' Angelo via Cinthia, I-80126 Napoli, Italy

[2] CNR-SPIN, Complesso Monte Sant'Angelo via Cinthia, I-80126 Napoli, Italy

[3] Materials Science and Technology Division, Oak Ridge National Laboratory, 1 Bethel Valley Rd., Oak Ridge, TN 37831, USA

[4] CNR-SPIN and Dipartimento di Fisica, Politecnico di Milano, Piazza Leonardo da Vinci 32, I-20133 Milano, Italy

[5] Laboratoire Charles Coulomb, UMR 5221, CNRS, Université Montpellier 2, F-34095 Montpellier, France

[6] CNR-SPIN and Dipartimento di Fisica, Università di Genova, Via Dodecaneso 33, I-14146 Genova, Italy

[7] Swiss Light Source, Paul Scherrer Institut, CH-5232 Villigen PSI, Switzerland

[8] Institute of Condensed Matter Physics, Ecole Polytechnique Fédérale de Lausanne, CH-1015 Lausanne, Switzerland

[9] Dipartimento di Ingegneria dell'Informazione, Seconda Università degli Studi di Napoli (SUN), Aversa (CE), Italy

Corresponding Authors

* daniela.stornaiuolo@fisica.unina.it

** marco.salluzzo@spin.cnr.it

© 2015 Macmillan Publishers Limited. All rights reserved

Supplementary Methods and data: HRTEM and EELS of LAO/ETO/STO

Simultaneous spectroscopy and high angle annular dark field (HAADF) imaging was conducted on samples that were thinned to electron transparency in cross sectional geometry, using conventional polishing and ion milling techniques. Samples were first polished with a high precision polishing machine down to a thickness of 10-20 μm avoiding any contact with moisture, and then ion milled after cooling to LN_2 temperature. Typical ion milling voltage and current conditions were 3.5 keV and 4 mA. A final cleaning step was performed at 0.5 keV and 3 mA for 5-10 minutes.

The microscope used for this study was a Nion UltraSTEM 200^{TM} operating at 200 kV [S1], equipped with a second generation 5th-order probe aberration corrector, a cold field emission electron gun, and a Gatan Enfinium dual EELS spectrometer. This microscope routinely achieves a spatial resolution of 0.6 Å for HAADF imaging. HAADF inner collection half-angle was 68 mrad, the probe convergence half angle was 30 mrad. The maximum EELS energy resolution was 300 meV, and the EELS collection angle was 33 mrad. Atomically resolved spectrum images were acquired using a grid of 40 X 110 pixels, a dwelling time of 0.01 s and a dispersion of 0.25 eV/ch. The Enfinium dual acquisition technology allowed us to acquire simultaneously all the following edges: Ti-$L_{2,3}$, La-$M_{4,5}$, and Eu-$M_{4,5}$. The zero loss spectra were also acquired subsequently. The thickness of the TEM foil was 0.35 mean free paths in the region analyzed.

The EELS spectra were processed in the following way: the background was removed using a power law function, plural scattering effects were removed by de-convolution of the low loss spectrum using the Fourier-ratio method [S1] implemented in Digital Micrograph. To obtain the relative concentration of some of the elements, the "Quantification" routine of Digital Micrograph based on the procedure developed by Egerton [S2] was used and cross sections were modeled with Hartree-Slater functions.

We find that Eu is mainly in the Eu^{2+} oxidation state ($4f^7$) in the ETO layers, implying, according to Hund's rules, an $^8S_{7/2}$ ground state (L=0, S=7/2, J=7/2), thus a high spin magnetic state. A small fraction of Eu^{3+} in ETO might be present to allow charge neutrality. EELS data show indeed a small shoulder which can be attributed to Eu^{3+}. From the integral of the shoulder, convoluted with the remaining part of the spectra, we establish an upper limit of the Eu^{3+} contribution of the order of 5% per unit cell, i.e. at the limit of the EELS sensitivity. However, Eu^{3+} ($4f^7$, $^7F_0$, L=3, S=3, J=0) is non-magnetic, thus the ETO layer magnetic moment is totally due to the Eu^{2+} ions.

The ETO and STO layers are characterized by a small fraction of La-substitution. In particular, we find an upper limit for the La-doping of 12% ± 5% in the interfacial ETO-layer and 10% ± 5% in the second layer. Finally, the fraction of La in the first SrO layer belonging to STO is lower than 10% ± 5%. Combining EELS and XMCD data ultimately we find an upper limit of La-doping of ETO in LAO(10uc)/ETO(2uc)/STO heterostructures of 6% (see Supplementary Note 1). Additionally, some non-magnetic Eu^{3+} replaces La in the $LaAlO_3$ film. The concentration of Eu relative to La is at most 20% ± 5% in the first LAO plane and vanishes within three unit cells of LAO.

The amount of La/Sr and Al/Ti substitution in LAO/STO q2DEG found in ref. [S3] and in ref. [19] of the main text is more than 25%. Thus the LAO/ETO/STO heterostructures are characterized by structural and chemical order close to the one experimentally designed and comparable to that one of the best LAO/STO films available.

© 2015 Macmillan Publishers Limited. All rights reserved

Supplementary Data: XMCD spectra vs. magnetic field, simulated XMCD spectra and supplementary XMCD data on LAO/STO heterostructures

In Fig.S2 we show a set of XMCD spectra at the Ti-$L_{2,3}$ and Eu-$M_{4,5}$ edges measured at 2K as function of the magnetic field on a LAO(10uc)/ETO(2uc)/STO heterostructure. The data show that the Ti- and Eu- XMCD spectra have opposite signs and follow the same magnetic field behavior. The Ti- spectral shape is dominated by Ti^{4+}-$3d^0$ features, as shown by the atomic multiplet calculations in Fig.S2a performed using the same crystal field needed to fit the XLD data of Fig.1b and a negative exchange interaction. The Eu-XMCD (Fig.S2b), on the other hand, is perfectly reproduced assuming Eu in Eu^{2+} oxidation state and using a positive exchange parameter.

The XMCD spectral shape does not change substantially with the field. At low field (0.05 T, close to the remanence) a clear XMCD is observed at both Eu and Ti-edge. Note that the choice of 0.05 Tesla (and not zero nominal field) is due to the fact that superconducting coils built for high magnetic fields XAS/XMCD end stations (as that installed at the X-Treme beamline of SLS), frequently present trapped currents generating a non zero field for nominally zero field condition. Therefore, we decided to measure at finite and reliable fields, i.e. $\mu_0 H \geq 0.02$T.

In Fig.S3 we show a comparison between data acquired on LAO(10uc)/STO, LAO(10uc)/STO(2uc)/STO and LAO(10uc)/ETO(2uc)/STO at 6 Tesla in grazing incidence. We can see that, while some dichroism can be measured a 6T also on LAO/STO samples, the XMCD signal from the delta-doped LAO/ETO/STO is almost one order of magnitude larger.

Supplementary Methods: XMCD contribution of interface STO and ETO layers.

The expression of the Total Electron Yield (TEY) signal coming from a multilayer can be found in several textbooks and more explicitly in ref. [S4].
The Auger electron current emitted from atoms within the solid angle Ω of the element A in the i-th layer (placed between depths x_i and x_{i+1}) is:

$$I_{iA} = k_{iA} n_{iA} \int_{\Omega} \int_{x_i}^{x_i+1} \exp\left(-x/d\cos\alpha\right) d\Omega dx$$

, where k_{iA} is proportional to the primary electron beam current and to a coefficient determining the Auger electron emission, and d is the Auger electron Inelastic Mean Free Path (IMFP) in the sample. In Fig.S4 we show the ETO thickness dependence of the XMCD Ti-L_3 edge amplitude measured in normal incidence conditions at 2K and 6 Tesla on LAO(10uc)/ETO(2uc)/STO heterostructures. The data, normalized to the XAS intensity at L_3, are shown together with the theoretical profiles assuming a magnetic moment coming only from the ETO film and several possible choices of the IMFP d. The experimental data do not fall on a unique curve and the XMCD is not simply scaling with the ETO thickness. A linear extrapolation of the data to zero ETO thickness intersects the vertical axis at a finite value.

© 2015 Macmillan Publishers Limited. All rights reserved

These results show that the XMCD signal is not associated only to the ETO film. Thus other layers, belonging to the STO interface, contribute as well.

In order to verify this scenario, we consider the sample as divided along the interface normal in three regions, as shown in the inset of Fig.S5: the ETO film with thickness t_{ETO}, the interfacial STO layers with thickness t_{STO} and the bulk STO single crystal.

The total XAS intensity, determined from the total number of electrons coming out from the LAO/ETO/STO interface at the Ti-edge, I_{total}, is given by:

$$I_{total} \cong I_{ETO} + I_{STO}^{IF} + I_{STO}^{Bulk}$$

Taking into account the attenuation of the LAO layer (giving only an offset to the TEY XAS spectra), we have:

$$I_{ETO} = I_{ETO}^{\infty} \cdot \int_{-\pi/2}^{-\pi/2} \int_{0}^{t_{ETO}} \exp\left[-(x + t_{LAO})/\lambda_{x-ray}\right] \exp\left[-\left(t_{LAO} + x\right)/d\cos\alpha\right] sin\left(\pi/2\text{-}\alpha\right) d\alpha \; dx \quad \text{(eq.S1)}$$

$$I_{STO}^{IF} = I_{STO}^{\infty} \cdot \int_{-\pi/2}^{-\pi/2} \int_{t_{ETO}}^{t_{ETO}+t_{STO}} \exp\left[-(x + t_{LAO})/\lambda_{x-ray}\right] \exp\left[-\left(t_{LAO} + t_{ETO} + x\right)/d\cos\alpha\right] sin\left(\pi/2\text{-}\alpha\right) d\alpha \; dx$$

$$I_{STO}^{Bulk} = I_{STO}^{\infty} \cdot \int_{-\pi/2}^{-\pi/2} \int_{t_{ETO}+t_{STO}}^{\infty} \exp\left[-(x + t_{LAO})/\lambda_{x-ray}\right] \exp\left[-\left(t_{LAO} + t_{ETO} + t_{STO} + x\right)/d\cos\alpha\right] sin\left(\pi/2\text{-}\alpha\right) d\alpha \; dx$$

We have assumed for sake of simplicity an equal IMFP for each layer, i.e. $d_{LAO} = d_{STO} = d_{ETO} = d$. t_{LAO} and t_{ETO} are the thicknesses of the LAO and ETO films respectively, and $\lambda_{x\text{-}ray}$ is the penetration depth of the x-rays. I_{∞}^{ETO} and I_{∞}^{STO} are the number of electrons generated by ETO and STO respectively assuming an infinite thickness. We can safely consider at the Ti- $L_{2,3}$ edge $I_{\infty}^{ETO} = I_{\infty}^{STO}$.

To calculate the t_{ETO} thickness dependence of the XMCD signal, normalized to the total XAS intensity, we suppose that each Ti-layer in the ETO film and in the STO interfacial layers are characterized by the same magnetic moment. Thus:

$$XMCDnorm(t_{ETO}) = \frac{\left(I_{ETO}^{L} + I_{IF,STO}^{L}\right) - \left(I_{ETO}^{R} + I_{IF,STO}^{R}\right)}{I_{total}^{L} + I_{total}^{R}} \qquad \text{(eq.S2)}$$

, where $I_{ETO,STO}^{L,R}$ are the XAS intensities after absorption of left or right circularly polarized photons related to the different layers.

In Fig.S5 we show the comparison between experimental XMCD data vs. the ETO thickness and the theoretical curve from eq.S2. A reasonable agreement is obtained with an interfacial STO thickness contributing to the XMCD of t_{sto}=0.5 nm and a probing depth of d_{STO}=3.5 nm [S5]. The latter is a realistic value for d_{STO} and gives an optimal fit of the data.

We point out that the actual thickness of the STO interfacial layer characterized by a non-null Ti-XMCD is larger than 0.5 nm, since the assumption that each STO layer gives the same contribution to the XMCD of the ETO layers is very crude. An exponentially decaying XMCD signal within a distance of 3-4 unit cells in the STO is much more realistic.

© 2015 Macmillan Publishers Limited. All rights reserved

Supplementary Methods and Data: Magneto-resistance and Hall-effect Hysteresis

In order to analyze the low field magneto-transport, we have performed measurements in a set-up equipped with a low-field superconducting magnet mounted in a multiple shielded environment, filtered lines, and a homemade non-magnetic OFHC-Cu (Oxygen Free High Conductivity-Copper) sample holder. This set-up is used also for the study of the Josephson effect and for the measurement of Superconducting Quantum Interference Devices (SQUID). The maximum magnetic field applied during this experiment was ± 0.3T. All the curves in Fig.S6 have been measured several times, with magnetic field sweeping at a speed of 0.005 T/min, and a careful control of the temperature stability.

We performed measurements as function of the gate voltage and as a function of the temperature above (650 mK) and below the onset of the superconducting transition (R_{sq}=90% of the normal state resistance).

Data acquired at V_g=+30 V in the normal state (at which the samples show all the signatures of a FM behavior), show interesting R_{xx} *vs.* $\mu_0 H$ magnetoresistance hysteresis, with the resistance being lower after the magnetic field is swept from zero to ±0.3 Tesla, as expected for a ferromagnet (Fig.S6a). For the same gate voltage, below the onset of the superconducting transition, the data show a dip around zero magnetic field due to superconductivity, and a hysteretic behavior of the resistance with similar characteristics compared to the data at 650 mK (Fig.S6b).

On the other hand, in data acquired at V_g=-30 V, with the sample not being anymore in the FM-state, but in a Kondo regime, and still showing superconductivity, we do not see any discernable hysteresis in both the superconducting and the normal state (Fig.S6c and Fig.S6d).

Similar conclusions can be drawn by looking at the Hall effect data. The Hall resistivity is hysteretic only in the FM state, both above and below Tc-onset (Fig.S6e and Fig.S6f), while no hysteresis is observed at V_g=-30 V in the Kondo regime (Fig.S6g and Fig.S6h).

The results obtained in the normal state are in agreement with all the other evidences for a transition from a FM to a non-FM system as function of the gate voltage.

Supplementary Methods and Data: Analysis of the Hall-effect data

A non-linear Hall effect in LAO/STO heterostructures has been measured by Joshua et al. (ref. [25] of the main text) and by other groups (e.g. C. Bell et al. [S6], M. Ben Shalom et al. [S7], S.Lerer et al. [S8], and A. Fete et al. [S9]). In these works, Rxy vs. μ_0H shows a decrease in the slope at increasing magnetic field. This behavior is related to the presence of electrons with different mobility in the q2DES, whose relative contribution to the transport varies with the magnetic field. The non-linearity associated to a two-band transport is modelled by the following equation (ref. [25] of the main text):

© 2015 Macmillan Publishers Limited. All rights reserved

$$R_H = R_\infty + \frac{R_0 - R_\infty}{1+\left(H/H_W\right)^2} \qquad \text{eq.S4}$$

where

$$R_0 = \frac{n_1\mu_1^2 + n_2\mu_2^2}{\left(n_1\mu_1 + n_2\mu_2\right)^2} \qquad R_\infty = \frac{1}{n_1+n_2} \text{ and } \quad H_W = \frac{n_1\mu_1 + n_2\mu_2}{\left(n_1+n_2\right)\mu_1\mu_2}$$

Our data at 1.8 K, for $V_g > -30$V, show two non-linearities, i.e. a change in the slope of the Rxy vs. $\mu_0 H$ data, with opposite curvatures: one at low field ($\mu_0 H = 3$T) and the other at high field ($\mu_0 H > 8$T).

We first analyze the low field non-linearity. As shown in Figs 4a and 4b of the main text, our R_{xy} vs. $\mu_0 H$ data for $V_g > -30$V, corresponding to a carrier concentration $n_c = 1.9\ 10^{13}$ cm^{-2} determined from the Hall coefficient at 12 Tesla, are characterized by an increase in the R_{xy}-slope at $\mu_0 H = 3$T. We relate this non-linearity to the Anomalous Hall effect (AHE) taking place in FM systems characterized by an intermediate/low carrier density and a non-negligible spin-orbit coupling. The fit of these data using a two band model (eq.S4), indeed, gives unphysical parameters and in particular a total number of carriers (n_1+n_2) lower than the carriers in the first band (n_1). This is not surprising since this low field non-linearity has an opposite curvature compared to that shown for LAO/STO in ref. [25] of the main text and in ref. [S6-S9]. Another striking difference between the low field R_{xy} vs. $\mu_0 H$ data presented in our manuscript and those shown in ref. [25] is the carrier concentration behavior. In LAO/ETO/STO once the R_{xy} vs. $\mu_0 H$ curves become kinked at low field, the kink position does not change with the gate voltage (Fig.4d of the main text) because it is determined by the saturation field of the out of plane magnetization. In LAO/STO, on the other hand, the field position of the non-linearity in R_{xy} vs. $\mu_0 H$ varies considerably, decreasing from 14 to 2T for a carrier density increasing from 1.8 to $2.6\text{x}10^{13}$ cm^{-2} (ref. [25] of the main text). In conclusion, the low field non-linear Hall effect we measure in LAO/ETO/STO heterostructures is not compatible with a multiple carrier scenario, but is similar to that one found in ferromagnetic, electron doped, ETO films (see ref. [20] and ref. [26] of the main text).

We now turn to the high field non-linearity in our R_{xy} vs. $\mu_0 H$. At carrier density larger than n_c, our R_{xy} vs. $\mu_0 H$ are characterized by a slight downward curvature for $\mu_0 H > 8$T. This is more evident in the $R_H(\mu_0 H)/R_H$(12T data) shown in Fig.S7a. The high field non-linearity in our data measured at 1.8K is much less pronounced than that shown for the LAO/STO system. The reason is that below T_{FM}, the low field AHE can mask the high field non-linearity. As shown in Fig.S7b, above T_{FM} the Hall-effect curvature at high field becomes more evident, while the low-field one disappears. We used eq.(S4) to fit the $T > T_{FM}$ Hall-effect data, as shown in Fig.S7b for the case of $V_g = +32$V (black line). A good fit is obtained with the following parameters: $n_1 = 2.1\text{x}10^{13}$cm^{-2} and $\mu_1 = 300$ cm^{2}V^{-1}s^{-1} for the first type of carrier, and $n_2 = 9.6\text{x}10^{12}$cm^{-2} and $\mu_2 = 730$ cm^{2}V^{-1}s^{-1} for the second.

The analysis of the high temperature data in terms of two-bands gives a clear evidence that the second non-linearity is related to the filling of a second band, i.e. the 3dxz,yz band. Thus, the data show that the multiband conduction appears just above n_c.

© 2015 Macmillan Publishers Limited. All rights reserved

Supplementary Magneto-conductance data

The study of the magneto-conductance can provide information about the scattering mechanisms acting in 2D systems and their competition. This analysis was used in literature to reveal the presence of spin-orbit coupling (SOC) in the q2DES at the LAO/STO interface and to trace its evolution as a function of the carrier concentration and temperature (ref. [5, 6] of the main text and ref. [S7], [S8]).

In Fig.S8 we show a set of differential conductance $\Delta\sigma=\sigma(H)-\sigma(0)$ curves, in units of the quantum of conductance $\sigma_0 = e^2/\pi h$, acquired at 1.8K on a LAO(10uc)/ETO(2uc)/STO heterostructure below and above V_g=-30V, i.e. below and above the critical carrier density n_c=1.9 10^{13} cm^{-2}. σ is the 2D-conductance and H is the magnetic field applied perpendicular to the interface. The data show, at low field, a negative behavior of the magneto-conductance typical of weak anti-localization due to spin-orbit scattering. For field larger than 4T, the curves measured at higher doping display a parabolic-like behavior, due to a contribution from classic magneto-conductance under high magnetic field [S10].

In Fig.S9 we show the analysis of the differential magneto-conductance measured at V_g=0V, corresponding to a carrier concentration n_{2D} of about 2.5x10^{-13} cm^{-2} and T=1.8 K. We fit the experimental data using the model proposed by Maekawa-Fukuyama (MF) following ref. [5, 6] of the main text and ref. [S11]-[S12]:

$$\frac{\Delta\sigma(H)}{\sigma_0} = \Psi\left(\frac{H}{H_i + H_{so}}\right) + \frac{1}{2\sqrt{1-\gamma^2}}\Psi\left(\frac{H}{H_i + H_{so}\left(1+\sqrt{1-\gamma^2}\right)}\right) - \frac{1}{2\sqrt{1-\gamma^2}}\Psi\left(\frac{H}{H_i + H_{so}\left(1-\sqrt{1-\gamma^2}\right)}\right) \qquad \text{(eq.S3)}$$

, where $\Psi(x) = \ln(x) + \psi\left(\frac{1}{2}+\frac{1}{x}\right)$ with ψ the digamma function and $\gamma = g\mu_B H / 4eDH_{so}$ with μ_B the Bohr magneton and e the electron charge. H_i and H_{so} are the inelastic and spin-orbit characteristic fields, respectively. The fit is shown as a red line in Fig.S9 and gives the following values for the characteristic fields: H_i =0.03T and H_{so} =1.37T. These values are comparable with those found for the LAO/STO system for a similar carrier concentration and using the same model [S12].

© 2015 Macmillan Publishers Limited. All rights reserved

Supplementary Note 1

In order to get an independent estimation of the upper limit of La-doping in ETO, we have used the Eu-XMCD data as function of the ETO thickness. In case of strong interfacial La/Eu intermixing, we should expect a substantial increase of the XMCD signal (or of the magnetic moment) as function of the ETO thickness. Indeed, it is presumable that thicker films have a lower fraction of La replacing Eu in the whole ETO film. The thickness dependence of the XMCD is then expected to be:

$$XMCD\left(t_{ETO}\right) = XMCD(\infty)\cdot\left(1 - y/t_{ETO}\right) \qquad \text{eq. S5}$$

, where y is the fraction of La replacing Eu in the first interfacial layer. Please note that a similar formula is obtained assuming y to be the La-doping/per unit cells.
From a fit of the data using eq.S5 we get y=0.12. Thus for a LAO/ETO/STO heterostructure containing 2uc ETO film, the overall La doping is 0.12/2 =0.06 per unit cell. This result is consistent with EELS and STEM data and gives a more precise estimation of the La/Eu substitution in ETO.

Supplementary Note 2

In the $L_{2,3}$ edge x-ray absorption spectroscopy technique, a 2p electron is excited to the empty 3d states of the absorbing ion, living one core-hole which strongly perturb the system through Coulomb interaction with the 3d electrons (both with the excited electrons and with the valence electrons). For this reason, XAS is an extremely powerful tool to get the chemical oxidation state of a transition metal in a solid, as defined by the number of electrons bound to the absorbing ion. The valence electrons, by definition, are not bound to the absorbing ions but are shared with various degrees of covalence to the neighbor bonding ions. From this point of view, even in formally (or nominal) Ti^{4+} compounds, the effective oxidation state of Ti is not 4+, but is lower, due to the partial charge transfer of O2p electrons to Ti3d states. Conversely, electrons in the 3d-Ti bands do not necessarily show up in the XAS spectra as purely Ti^{3+}. Indeed, we expect the electrons filling Ti 3d-bands being either itinerant or somewhat localized, but still retaining the character of the highly dispersive 3d-bands (3d bands are strongly dispersive according to ARPES data available for LAO/STO [S13]). The presence of these $3d^1$ states will not necessarily show up in the XAS spectra with the typical signatures of Ti^{3+} XAS/XMCD spectra (i.e. of Titanium in strictly ionic limit behaving like a Ti^{3+}). Indeed, while the experimental XAS data for Ti^{4+} and Ti^{3+} compounds ($SrTiO_3$ and $LaTiO_3$, where Ti are in nominal Ti^{4+} and Ti^{3+} oxidation states, respectively) are very well reproduced by atomic multiplet scattering theory, in the mixed valence compounds the situation is very different.

This has been shown theoretically in the case of $La_{0.5}Sr_{0.5}TiO_3$ [S14], where departures from the localized atomic-like scenario (in which the two separate Ti^{3+} and Ti^{4+} contributions are added incoherently) effectively take place considering adequate covalence (hybridization) parameters. In our system, Ti-3d states are hybridized with Eu-4f and with O-2p orbitals. In other words, in the case of mixed or fluctuating valence

© 2015 Macmillan Publishers Limited. All rights reserved

compounds one should expect deviations from the pure ionic limit. This possibly suggests that the departure from the purely ionic picture can be so severe to make XAS and XMCD spectra resembling that one of a pure $3d^0$ system, even if the density of $3d^1$ electrons is not negligible.

We would like also to point out that, assuming the polar catastrophe scenario valid, the charges transferred to the interface atomic layers should amount to 0.5 electrons /square unit-cell distributed at the interface. Since the probing depth is about 10uc, (2uc of ETO + 8 uc of STO), the ratio between $3d^0$ and $3d^1$ states probed is lower than 0.05. It is then reasonable that the $3d^1$ features can be masked, because of the large XMCD signal coming from the majority of empty spin-split $3d^0$ states (even if the XMCD of a $3d^0$ system, theoretically, is much lower than that one of a $3d^1$ system).

In our case, the XMCD data measured on the Ti $L_{2,3}$ edge show essentially two contributions: one coming from the majority titanium ions in an oxidation state close to 4+, i.e. a $3d^0$ like contribution, and another from $3d^1$-electrons, including itinerant and localized electrons.

The first contribution is dominant in the shape of the XMCD, and is reproduced by atomic multiplet calculations assuming a $3d^0$ ground state and the presence of a negative exchange interaction, which split the 3d bands globally [see Fig.S2]. Another contribution comes from the $3d^1$ electrons and is responsible for finite spin and orbital moments.

The orbital moment, in particular, is quite large. As a comparison, we consider the case of $LaTiO_3$, where the Ti valence is purely Ti^{3+} in the whole lattice. M. Haverkort, et al., (ref. [22] of the main text), obtained an experimental value of the orbital moment in $LaTiO_3$ of -0.08 μ_B/Ti associated to the residual crystal field splitting of the t_{2g} states. Theoretical estimations of the orbital moment in $LaTiO_3$, with predicted crystal field similar to our case, on the other hand, give a value of -0.24 μ_B/Ti [S15]. Using these values and our data we get an idea of the electron density contributing to the orbital moment: it is 0.045/0.08=0.6 electrons/Ti, assuming the experimental value of $LaTiO_3$, 0.045/0.24=0.2 electrons/Ti considering the Solovyev et al. calculations [S15]. Taking into account that the density of itinerant carriers, measured by the Hall effect, is of the order of 0.05 electrons/Ti, these results show that all or a large part of the electrons in ETO and STO are spin polarized and contribute to the orbital moment.

This orbital moment cannot be attributed to the $EuTiO_3$ layers alone, providing further evidence of a Ti-magnetism in both ETO and STO layers. To be quantitative, with an average orbital moment of about -0.045 μ_B/Ti on a 3.5 nm thickness (the probing depth) and assuming the magnetic moment just coming from the 2 ETO layers, we get a conservative estimation of m_{orb} = -0.045*3.5/0.8 = -0.2 μ_B per Ti atom in the ETO layer. With a doping of 10% we can assume that only 10% of the Ti atom will contribute to the orbital moment, thus giving m_{orb} = 2 μ_B for these Ti atoms, which is clearly unrealistic.

© 2015 Macmillan Publishers Limited. All rights reserved

Supplementary References

[S1] Dellby, et al. Dedicated STEM for 200 to 40 keV operation. *Eur. Phys. J. Appl. Phys.* 5**4,** 33505 (2011).

[S2] R. F. Egerton. Electron energy loss spectroscopy in the transmission electron microscope. Second Edition, Plenum Press, New York (1996).

[S3] Willmott, P. *et al.* Structural Basis for the Conducting Interface between $LaAlO_3$ and $SrTiO_3$. *Phys. Rev. Lett.* **99,** 155502 (2007).

[S4] Mróz, S. & Mróz, A. Auger electron spectroscopy in the investigation of ultrathin films in molecular beam epitaxy. *Thin Solid Films* **367,** 126–133 (2000).

[S5] Frazer, B. H., Gilbert, B., Sonderegger, B. R. & De Stasio, G. The probing depth of total electron yield in the sub-keV range: TEY-XAS and X-PEEM. *Surface Science* **537,** 161–167 (2003).

[S6] Bell, C. *et al.* Dominant Mobility Modulation by the Electric Field Effect at the $LaAlO_3/SrTiO_3$ Interface. *Phys. Rev. Lett.* **103,** 226802 (2009).

[S7] Ben Shalom, M., Sachs, M., Rakhmilevitch, D., Palevski, A. & Dagan, Y. Tuning Spin-Orbit Coupling and Superconductivity at the $SrTiO_3/LaAlO_3$ Interface: A Magnetotransport Study. *Phys. Rev. Lett.* **104,** 126802 (2010).

[S8] Lerer, S., Ben Shalom, M., Deutscher, G. & Dagan, Y. Low-temperature dependence of the thermomagnetic transport properties of the $SrTiO_3/LaAlO_3$ interface. *Phys. Rev. B* **84,** 075423 (2011).

[S9] Fête, A. *et al.* Growth-induced electron mobility enhancement at the $LaAlO_3/SrTiO_3$ interface. *Appl. Phys. Lett.* **106,** 051604 (2015).

[S10] Yuan, H., et al. Zeeman-Type Spin Splitting Controlled by an Electric Field. Nat. Phys. **9**, 563 (2013).

[S11] Maekawa, S., Fukuyama, H. Magnetoresistance in Two-Dimensional Disordered Systems: Effects of Zeeman Splitting and Spin-Orbit Scattering. Journal of the Physical Society of Japan, **50**, 2516 (1981).

[S12] Fête, A., Gariglio, S., Caviglia, A.D., Triscone, J.-M., & M. Gabay. Rashba induced magnetoconductance oscillations in the $LaAlO_3$-$SrTiO_3$ heterostructure. Phys. Rev. B **86**, 201105 (2012).

[S13] Cancellieri, C. *et al.* Doping-dependent band structure of $LaAlO_3/SrTiO_3$ interfaces by soft x-ray polarization-controlled resonant angle-resolved photoemission. *Phys. Rev. B* **89,** 121412 (2014).

© 2015 Macmillan Publishers Limited. All rights reserved

[S14] Gupta, S. S., Wadati, H. & Sawatzky, G. A. The importance of inter-site coherences in the X-ray absorption spectra of mixed-valent systems. *Europhys. Lett.* **93,** 47008 (2011).

[S15] Solovyev, I. V. Lattice distortion and magnetic ground state of $YTiO_3$ and $LaTiO_3$. *Phys. Rev. B* **69,** 134403 (2004).

© 2015 Macmillan Publishers Limited. All rights reserved

Supplementary Figure Captions

Figure S1. (a) Z-contrast STEM image of delta-doped LAO(10uc)/ETO(2uc)/STO heterostructure (raw data). The yellow dashed lines indicate the TiO_2/EuO and the TiO_2/LaO interfaces according to EELS chemical map. Elemental EELS spectra obtained from the integrated intensities for (b) Eu, (c) La, (d) Ti) edges. (e) Overlay of (b), (c) and (d).

Figure S2. (a) Ti $L_{2,3}$ edge and (b) Eu $M_{4,5}$ edge XMCD spectra as function of the magnetic field of LAO(10uc)/ETO(2uc)/STO heterostructures. The spectra measured in grazing incidence conditions at 2K are compared to atomic multiplet calculations performed using the CTM4XAS code. The calculated Ti–XMCD (black lines) is obtained using a Ti^{4+}-$3d^0$ ionic configuration and a negative exchange interaction of -10 meV. The Eu-XMCD, is calculated using Eu in Eu^{2+} oxidation state and a positive exchange parameter. A constant offset is applied to the data for visualization.

Figure S3. Ti $L_{2,3}$ edge XMCD spectra on LAO(10uc)/ETO(2uc)/STO, LAO(10uc)/STO non-annealed in O_2, LAO(10uc)/STO annealed in O_2 and LAO(10uc)/STO(2uc)/STO grown in the same condition of the LAO/ETO/STO heterostructures. A constant offset is applied to the data for visualization. The spectra are measured in grazing incidence conditions, at 2K and 6T.

Figure S4. ETO thickness dependence of the XMCD Ti-L_3 edge signal (black circles) normalized to the XAS intensity. Continuous lines are calculated profiles assuming only the ETO film contributing to the XMCD. The different color lines correspond to different IMFP from 0.5 nm to 4.5 nm (0.5 nm step). The inset shows a magnification of the low thickness region and the linear extrapolation of the experimental data to zero (dashed red line).

Figure S5. Comparison between experimental XMCD data (normalized to Ti-L_3) vs. the thickness of the ETO delta-doping layer, and calculations from eq. S2 with an interfacial thickness of the STO layer of 0.5 nm contributing to the total signal (black full line). The black dashed lines are the calculated profiles assuming that only the ETO layers are magnetic (d is the IMFP). As shown in the inset, the sample is considered as divided along the interface normal in three regions.

Figure S6. a-d Magneto-resistance data around zero field measured at 650 mK (a and c) and below the SC transition (b and d) at Vg= +30 V (left) and Vg=-30 V (right). f-h Hall-effect data around zero field measured at 650 mK (e and g) and below the SC transition (f and h) at Vg= +30 V (left) and Vg=-30 V (right).

© 2015 Macmillan Publishers Limited. All rights reserved

Figure S7. Gate voltage dependence of the Hall resistance R_H normalized to the value a 12 Tesla. The data are vertically displaced by a fixed amount of 0.05. (b) Hall effect data measured at V_g=+32V at 1.8K (violet line) and 20 K (above $T_{FM,}$ orange line), and fit of the 20 K data using a two-bands model of eq.S4 (black line). In the inset we show a zoom of the high field part of the data. The dashed lines are linear fit of the intermediate field range (3T<H<6T), which highlight the non-linearity at high fields (H>8T). This high field non-linearity is visible in both curves and is more pronounced in the orange one measured at 20K.

Figure S8. Set of differential magneto-conductance data acquired at 1.8 K with the field perpendicular to the interface as function of the gate voltage below and above n_c.

Figure S9. Differential magneto-conductance of the LAO/ETO/STO system measured at V_g=0V and T=1.8K in perpendicular magnetic field. The red line is the fit performed using the MF model.

© 2015 Macmillan Publishers Limited. All rights reserved

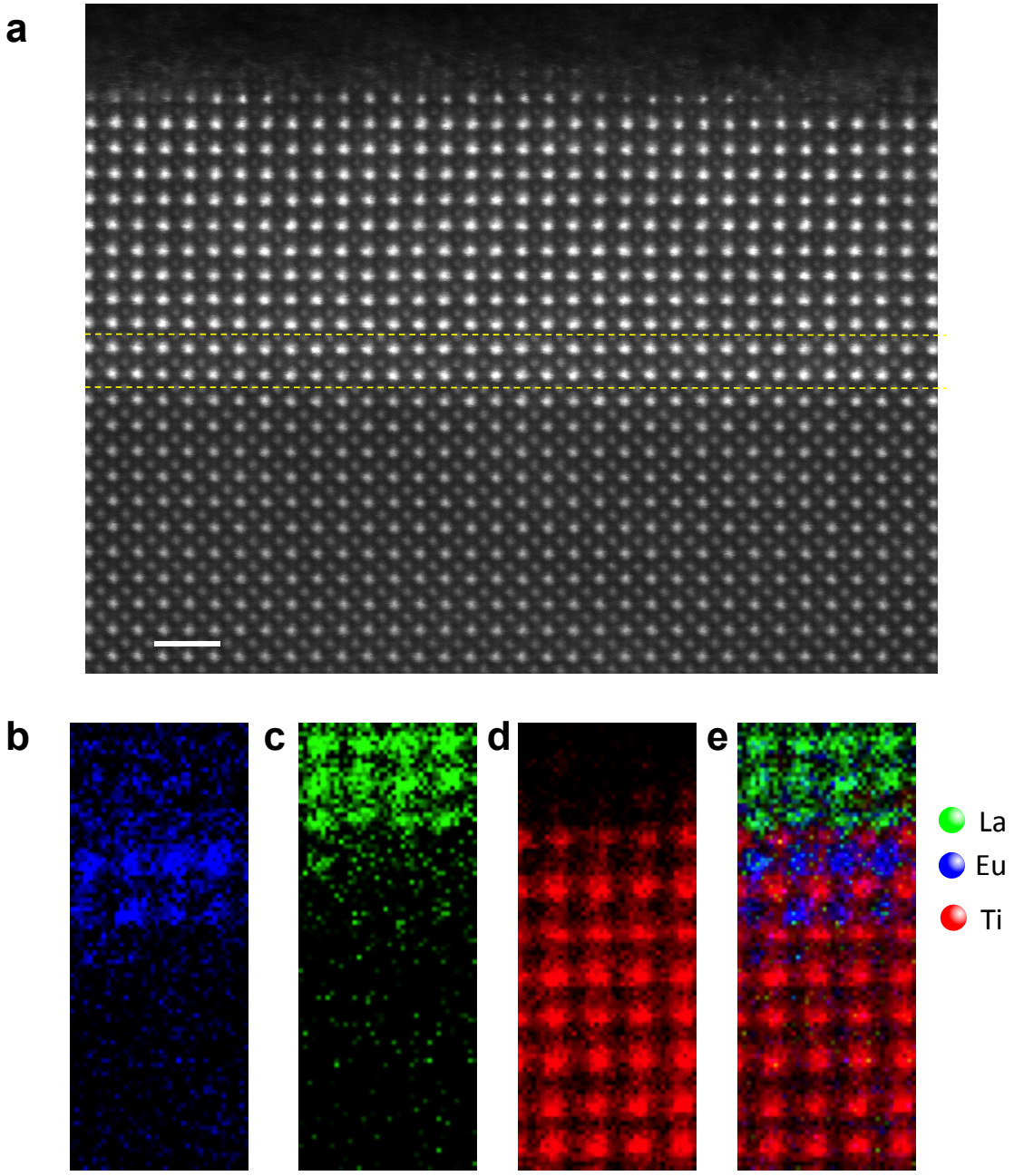

Figure S1

© 2015 Macmillan Publishers Limited. All rights reserved

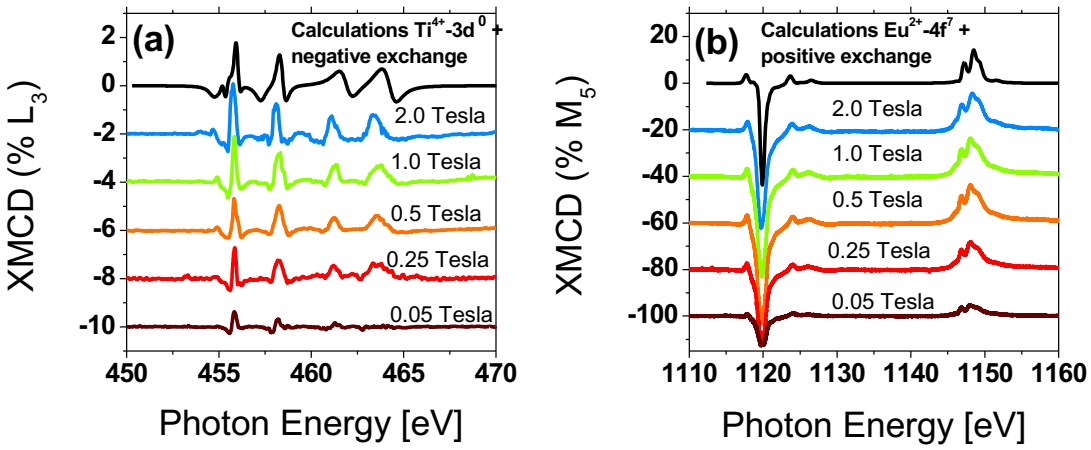

Figure S2

© 2015 Macmillan Publishers Limited. All rights reserved

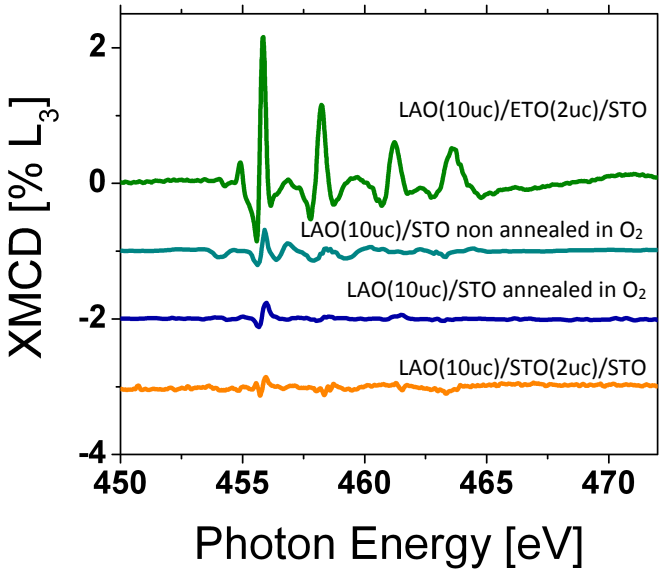

Figure S3

© 2015 Macmillan Publishers Limited. All rights reserved

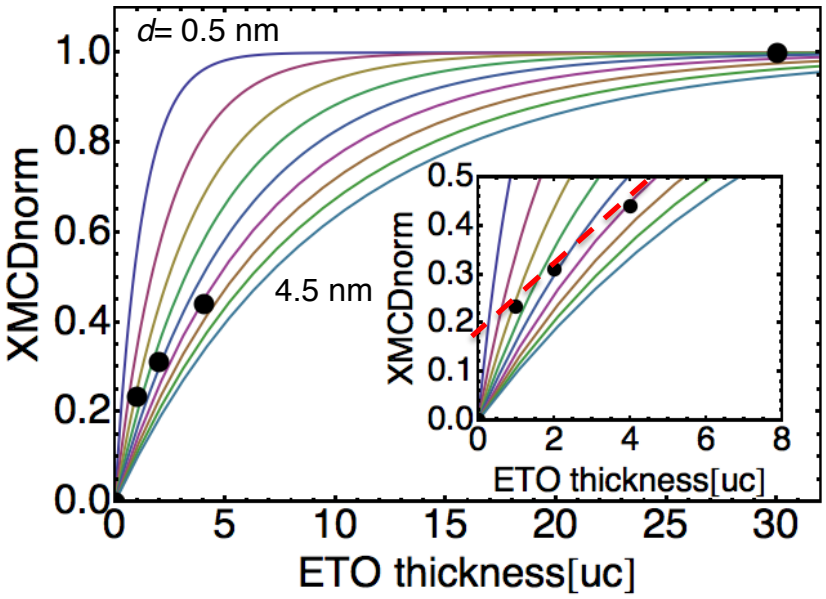

Figure S4

© 2015 Macmillan Publishers Limited. All rights reserved

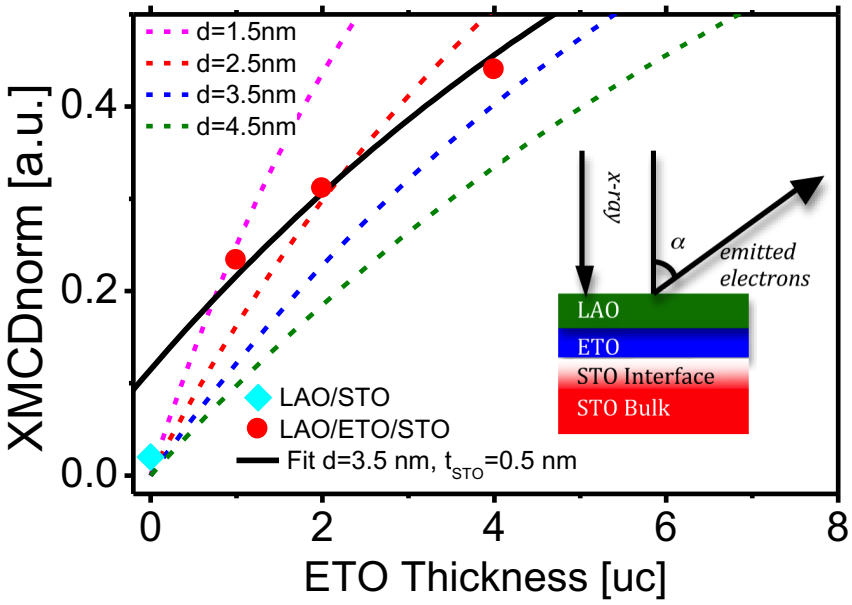

Figure S5

© 2015 Macmillan Publishers Limited. All rights reserved

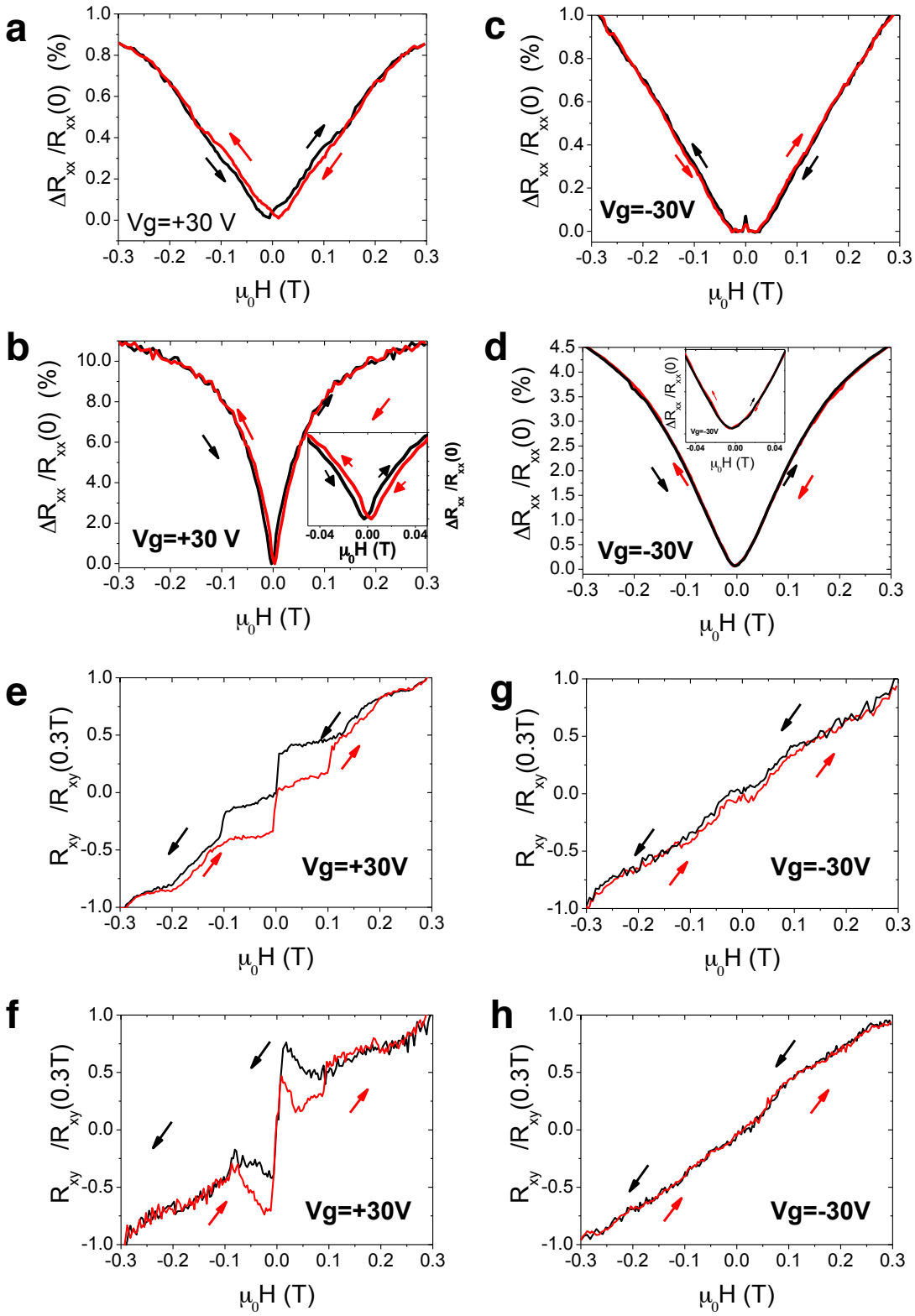

Figure S6

© 2015 Macmillan Publishers Limited. All rights reserved

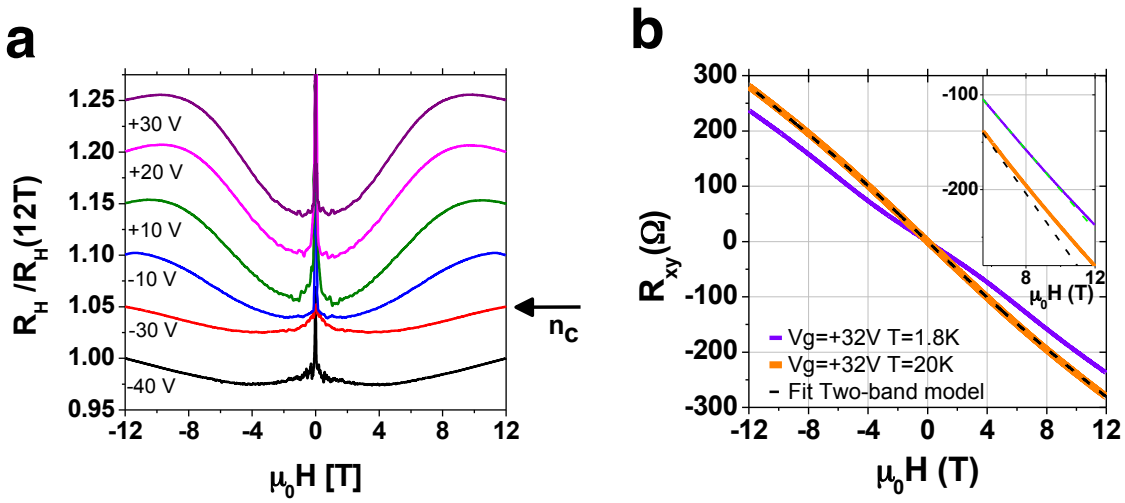

Figure S7

© 2015 Macmillan Publishers Limited. All rights reserved

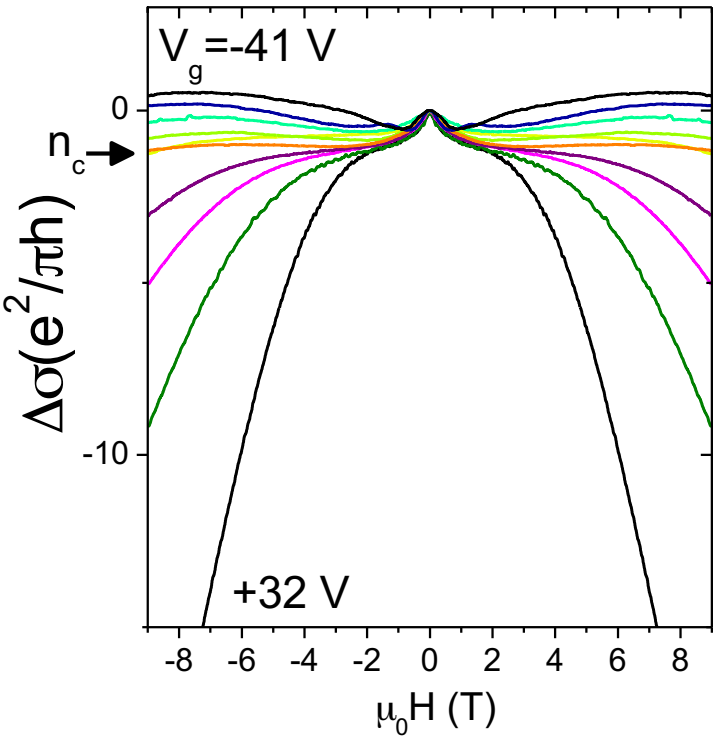

Figure S8

© 2015 Macmillan Publishers Limited. All rights reserved

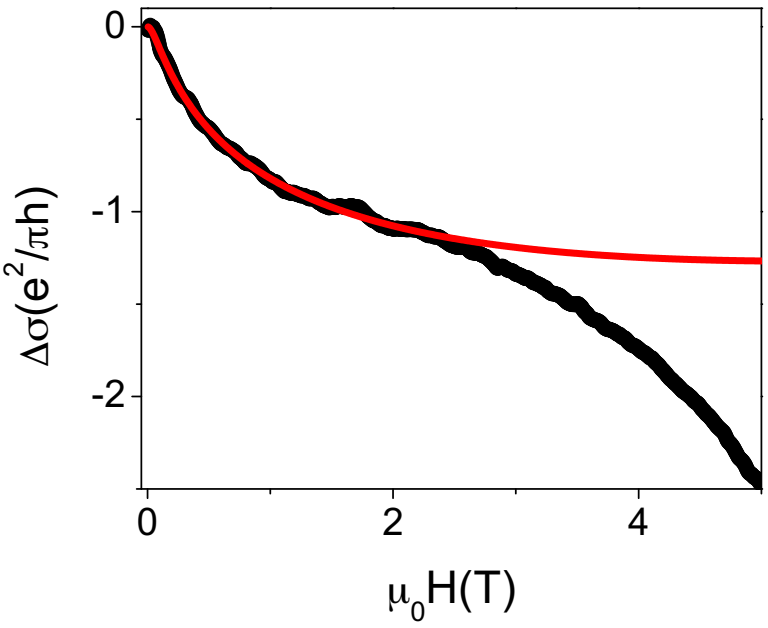

Figure S9

© 2015 Macmillan Publishers Limited. All rights reserved